

A preconditioned Riemannian conjugate gradient method for computing the ground states of arbitrary-angle rotating Bose-Einstein condensates

Qingzhou Shu^a, Qinglin Tang^a, Shaobo Zhang^{b,*}, Yong Zhang^b

^a School of Mathematics, Sichuan University, Chengdu, 610065, China

^b Center for Applied Mathematics and KL-AAGDM, Tianjin University, Tianjin, 300072, China

ARTICLE INFO

Keywords:

Bose-Einstein condensates
Arbitrary-angle rotation
Ground states
Preconditioned Riemannian conjugate gradient method
Bent vortex

ABSTRACT

In this article, we investigate the ground states (GS) of arbitrary-angle rotating Bose-Einstein condensates (BECs), modeled by the three-dimensional (3D) Gross-Pitaevskii equation (GPE). Firstly, we establish the existence results of the ground states with rigorous proof. Secondly, we propose a preconditioned Riemannian conjugate gradient (pRCG) method coupled with the Fourier pseudo-spectral discretization to compute the ground states numerically. A robust and efficient preconditioner together with an adaptive stepsize control strategy is proposed to accelerate the convergence. Thirdly, utilizing the pRCG algorithm, we study the ground state patterns in various settings extensively. Particularly, for the first time, we observe bent vortex lines, including U-shaped and S-shaped vortex lines, in the elongated BEC with arbitrary-angle rotation. We also study how the bent vortex line patterns change with the angle between the rotation axis and the elongated direction in detail. Lastly, we perform a comprehensive numerical study to confirm the spectral accuracy and showcase the great computational efficiency, and study the influences of physical parameters on GS patterns of BECs with arbitrary-angle rotation.

Contents

1. Introduction	2
2. Existence of the ground state	3
3. Numerical method	4
3.1. Discretization and the manifold geometry of the minimization problem	4
3.2. A preconditioned Riemannian conjugate gradient method	6
4. Numerical results	7
4.1. Accuracy and efficiency test	8
4.2. New vortex structure in anisotropic BEC	9
4.3. GS patterns under different model parameters	11
5. Conclusion	13
CRedit authorship contribution statement	14

* Corresponding author.

E-mail addresses: qingzhou_shu@stu.scu.edu.cn (Q. Shu), qinglin_tang@scu.edu.cn (Q. Tang), shaobo_zhang@tju.edu.cn (S. Zhang), Zhang_Yong@tju.edu.cn (Y. Zhang).

<https://doi.org/10.1016/j.jcp.2024.113130>

Received 24 March 2024; Accepted 19 May 2024

Available online 27 May 2024

0021-9991/© 2024 Elsevier Inc. All rights are reserved, including those for text and data mining, AI training, and similar technologies.

Declaration of competing interest	14
Data availability	14
Acknowledgements	15
References	15

1. Introduction

Bose-Einstein condensates (BECs) are a remarkable state of matter that have captivated researchers since their experimental realization in 1995 [5,17,22]. In BECs, particles such as ultra-cold atoms are cooled to temperatures close to absolute zero, causing them to occupy the same quantum state. This phenomenon gives rise to a unique, coherent state of matter with extraordinary quantum properties, which permits an intriguing glimpse into the macroscopic quantum world. Over the last 20 years, research on BECs has developed very rapidly in the fields of atomic, molecular, optics and condensed matter physics. Among them, particular attention has been paid to rotating BECs, where quantum vortices [1,18] are induced. The appearance of vortices is a mark of the superfluid nature of BECs and holds wide-ranging potential applications, spanning from astrophysics to atomic physics, optics and superfluid dynamics. Early experiments on rotating BECs focus on rotation along the z -axis, whereas real-world applications may require rotation at arbitrary angles. For instance, recently, a BEC confined by a rotating harmonic trap whose rotation axis is not aligned with any of its principal axes has been investigated [31]. In [30], the Thomas-Fermi theory was extended to harmonically trapped dipolar Bose-Einstein condensates, polarized by a continuously rotating field with the flexibility to be oriented at any angle to its rotation axis. BECs with arbitrary-angle rotation constitute a captivating subject within the realm of quantum physics [16,26,30,31,36,37].

At temperature T lower than the critical temperature T_c , the macroscopic behavior of a BEC in an arbitrary-angle rotational frame can be accurately captured by a complex-valued wave function $\psi(\mathbf{x}, t)$, whose evolution is governed by the dimensionless Gross-Pitaevskii equation (GPE) with an arbitrary angular momentum rotation term in three dimension (3D) [7,8]:

$$\begin{cases} i\partial_t\psi(\mathbf{x}, t) = \left[-\frac{1}{2}\Delta + V(\mathbf{x}) + \beta|\psi(\mathbf{x}, t)|^2\right]\psi(\mathbf{x}, t) - (\boldsymbol{\Omega} \cdot \mathbf{L})\psi(\mathbf{x}, t), & \mathbf{x} \in \mathbb{R}^3, \quad t > 0, \\ \psi(\mathbf{x}, 0) = \psi_0(\mathbf{x}), & \mathbf{x} \in \mathbb{R}^3. \end{cases} \tag{1.1}$$

Here, $\mathbf{x} = (x, y, z)^T$, t denote respectively the spatial and time variables, $\Delta = \nabla^2$ is Laplace operator with $\nabla := (\partial_x, \partial_y, \partial_z)^T$ the standard gradient operator, $\beta \in \mathbb{R}$ is a constant characterizes strength of short range two-body interaction in a condensate (positive for repulsive and negative for attractive). $V(\mathbf{x})$ is an external trapping potential usually taken as the harmonic oscillator type [12,13]

$$V(\mathbf{x}) = V_{\text{har}}(\mathbf{x}) := \frac{\gamma_x^2 x^2 + \gamma_y^2 y^2 + \gamma_z^2 z^2}{2}, \tag{1.2}$$

with γ_ν the trapping frequency in ν -direction ($\nu = x, y, z$). The rotation of the system is characterized by the term $\boldsymbol{\Omega} \cdot \mathbf{L} := \boldsymbol{\Omega}^T \mathbf{L}$, i.e. the inner product of the rotation frequency $\boldsymbol{\Omega}$ and angular momentum \mathbf{L} defined as

$$\boldsymbol{\Omega} = (\omega_x, \omega_y, \omega_z)^T, \quad \mathbf{L} = \mathbf{x} \times \mathbf{p} = \mathbf{x} \times (-i\nabla) =: (L_x, L_y, L_z)^T.$$

A simple calculation shows the angular momentum in ν -direction ($\nu = x, y, z$) reads as

$$L_x = -i(y\partial_z - z\partial_y), \quad L_y = -i(z\partial_x - x\partial_z), \quad L_z = -i(x\partial_y - y\partial_x). \tag{1.3}$$

In most experiments, the rotating axis is aligned parallel to the z -axis, hence leading to a rotation frequency $\boldsymbol{\Omega} = (0, 0, \omega_z)^T$. As such, the rotation term reduces to $\boldsymbol{\Omega} \cdot \mathbf{L} = \omega_z L_z$, with which the corresponding BEC system has been well studied. One can refer to [11] and references therein.

The time dependent GPE (1.1) conserves two important quantities: the total mass (or normalization)

$$N(\psi) := \|\psi(\cdot, t)\|_2^2 = \int_{\mathbb{R}^3} |\psi(\mathbf{x}, t)|^2 d\mathbf{x} = \|\psi(\cdot, 0)\|_2^2 = 1, \quad t \geq 0, \tag{1.4}$$

and the energy per particle

$$E(\psi) = \int_{\mathbb{R}^3} \left(\frac{1}{2} |\nabla\psi|^2 + V(\mathbf{x})|\psi|^2 + \frac{\beta}{2} |\psi|^4 - \psi^*(\boldsymbol{\Omega} \cdot \mathbf{L})\psi \right) d\mathbf{x}, \tag{1.5}$$

where ψ^* denotes the complex conjugate of ψ . The ground states (GS) of the arbitrary-angle rotating BEC is defined as follows [3,11,27]

$$\phi_g(\mathbf{x}) := \underset{\phi \in \mathbb{S}}{\operatorname{argmin}} E(\phi), \quad \text{with} \quad \mathbb{S} := \{ \phi(\mathbf{x}) \in L^2(\mathbb{R}^3) \mid \|\phi(\mathbf{x})\|_2 = 1, E(\phi) < \infty \}, \tag{1.6}$$

which is a non-convex minimization problem due to the constraint. It can also be defined as the stationary states of GPE (1.1) with the lowest energy, which then leads to a nonlinear eigenvalue problem [23,39].

For BECs with rotation axis parallel to z -axis, there have been extensive theoretical and numerical studies on the GS of such systems [3,4,8,9,11,12,15,23–25]. The difficulties in numerically computing the GS lie in the proper treatment of the constraint and in resolving the hyperfine vortex structure induced by rotation. For highly rotating and strongly nonlinear systems, GS is usually equipped with a vortex lattice and the energy landscape presents shallower minima. Hence, numerical schemes need to be accurate enough to capture those spatial-small-scale vortices and be of the capability to escape from most local shallower minima. Various numerical methods were developed based on solving the non-convex constrained optimization problems (1.6) or its correlated Euler-Lagrange equation. For the later approach, one can refer to [23,39] and references therein. The former approach includes methods such as those based on proper discretizations of gradient-type flows and their variants [6–8,12,19,20,28,41] as well as those based on direct minimizing the energy functional (1.5) [9,10,13,21,40,38]. Among them, the preconditioned Riemannian conjugated gradient (pRCG) methods [9,10,21], which treat problem (1.6) as an unconstrained minimization problem on Riemannian manifold, was numerically evidenced to be one of the best. With proper choice of the preconditioner and stepsize control strategy, which play a key role in the acceleration of the convergence process, the pRCG algorithm is shown to be accurate, efficient and robust for computing GS of rotating BECs, especially for those systems with fast rotation and strong nonlinearity [9,10].

However, for BECs with arbitrary-angle rotation, to our best knowledge, there is little literature yet developing numerical methods for its GS computation. Due to the 3D nature and possible hyperfine vortex-structure caused by the angle between the rotation axis and elongated direction of an anisotropic condensate, it is challenging to develop an efficient and robust numerical method to compute the GS of BEC with arbitrary-angle rotation. This motivates us to extend the pRCG method integrating with a Fourier pseudo-spectral method for spatial discretization, whose impressive performance has been evidenced for a system of rotation axis parallel to z -axis, to compute the GS of arbitrary-angle rotating BECs. Other objectives of this paper are as follows: (i) to provide the existence of the GS of arbitrary-angle rotating BECs. (ii) to explore the impacts of model parameters, such as the external trapping potential, the rotation and the nonlinear interaction strength, on the properties and patterns of GS. Specially, we investigate GS patterns with intriguing bent vortex structures versus the angle between the rotation axis and the elongated direction of a BEC [24,25].

The rest of the paper is organized as follows. In Section 2, we present existence results of the GS of arbitrary-angle rotating BECs with rigorous proofs. In Section 3, we propose a Fourier pseudo-spectral method to discretize the constrained optimization problem. We also introduce the manifold geometry structure of the discretized optimization problem, including the Riemannian gradient, Riemannian Hessian, retraction and vector transport. Based on this, a preconditioned Riemannian conjugate gradient (pRCG) method is proposed to solve the discretized optimization problem. In Section 4, we test the performance of the pRCG method, and apply it to investigate the GS patterns and vortex structures of BECs under various settings of physical parameters. Several conclusions are presented in Section 5.

2. Existence of the ground state

Existence results of the ground state for BECs with a rotating axis paralleled to z -axis are well-researched and one can refer to [14,33] and references therein. For the existence and simple properties of ground state for the arbitrary-angle rotating BEC, we have the following results:

Theorem 1. For systems with harmonic trapping potential (1.2), we have

- (1) If $\phi(x, y, z)$ is a ground state of $E_{\omega_x, \omega_y, \omega_z}(\phi)$, then $\phi(x, y, -z)$, $\phi(x, -y, z)$ and $\phi(-x, y, z)$ are ground states of $E_{-\omega_x, -\omega_y, \omega_z}(\phi)$, $E_{-\omega_x, \omega_y, -\omega_z}(\phi)$ and $E_{\omega_x, -\omega_y, -\omega_z}(\phi)$ respectively. Here, $E_{\omega_x, \omega_y, \omega_z}(\phi)$ denotes the energy for wave function ϕ with rotation frequency $\mathbf{\Omega} := (\omega_x, \omega_y, \omega_z)^T$.
- (2) For $\beta \geq 0$, there exists a ground state if the following matrix

$$A = \begin{pmatrix} \gamma_x^2 - (\omega_y^2 + \omega_z^2) & \omega_x \omega_y & \omega_x \omega_z \\ \omega_x \omega_y & \gamma_y^2 - (\omega_x^2 + \omega_z^2) & \omega_y \omega_z \\ \omega_x \omega_z & \omega_y \omega_z & \gamma_z^2 - (\omega_x^2 + \omega_y^2) \end{pmatrix} \quad (2.1)$$

is positive definite. Specially,

- (i) for an isotropic trapping potential, i.e. $\gamma_x = \gamma_y = \gamma_z = \gamma$, the ground state exists as long as $|\mathbf{\Omega}| < \gamma$;
- (ii) for the typical rotation frequency $\mathbf{\Omega} = (0, 0, \omega_z)^T$, the ground state exists when $|\omega_z| < \min\{\gamma_x, \gamma_y\}$, which is the same as that already established in [14,33].

Proof. The first conclusion is easy to check with a change of variables, therefore we choose not to present details here and shall focus on existence results of the ground state. Using a Householder transform $\mathbf{x} = P\bar{\mathbf{x}}$, we can map the rotation vector $\mathbf{\Omega}$ to \bar{z} -axis, i.e. $P(0, 0, |\mathbf{\Omega}|)^T = \mathbf{\Omega}$, where the orthogonal matrix P is symmetric and reads as follows

$$P = I_3 - \frac{1}{|\mathbf{\Omega}|(|\mathbf{\Omega}| - \omega_z)} \begin{pmatrix} \omega_x^2 & \omega_x \omega_y & \omega_x(\omega_z - |\mathbf{\Omega}|) \\ \omega_x \omega_y & \omega_y^2 & \omega_y(\omega_z - |\mathbf{\Omega}|) \\ \omega_x(\omega_z - |\mathbf{\Omega}|) & \omega_y(\omega_z - |\mathbf{\Omega}|) & (\omega_z - |\mathbf{\Omega}|)^2 \end{pmatrix}.$$

We then introduce a new wave function $\tilde{\phi}(\tilde{\mathbf{x}}) := \phi(\mathbf{x})$ using such Householder transform. Using the chain rule and vector cross product properties, we have

$$\begin{aligned} \nabla_{\mathbf{x}}\phi(\mathbf{x}) &= P\nabla_{\tilde{\mathbf{x}}}\tilde{\phi}(\tilde{\mathbf{x}}), & \Delta_{\mathbf{x}}\phi(\mathbf{x}) &= \Delta_{\tilde{\mathbf{x}}}\tilde{\phi}(\tilde{\mathbf{x}}), \\ \boldsymbol{\Omega} \cdot L\phi &= \boldsymbol{\Omega} \cdot \left[\mathbf{x} \times (-i\nabla_{\mathbf{x}}\phi) \right] = \boldsymbol{\Omega} \cdot \left[P\tilde{\mathbf{x}} \times (-iP\nabla_{\tilde{\mathbf{x}}}\tilde{\phi}) \right] = -\boldsymbol{\Omega} \cdot P \left[\tilde{\mathbf{x}} \times (-i\nabla_{\tilde{\mathbf{x}}}\tilde{\phi}) \right] \\ &= -P\boldsymbol{\Omega} \cdot \left[\tilde{\mathbf{x}} \times (-i\nabla_{\tilde{\mathbf{x}}}\tilde{\phi}) \right] = -(0, 0, |\boldsymbol{\Omega}|)^T \cdot \left[\tilde{\mathbf{x}} \times (-i\nabla_{\tilde{\mathbf{x}}}\tilde{\phi}) \right] \\ &= -|\boldsymbol{\Omega}|L_z\tilde{\phi}, \end{aligned}$$

with $L_z = -i(\tilde{x}\partial_{\tilde{y}} - \tilde{y}\partial_{\tilde{x}})$. The energy (1.5) is then equivalent to the following

$$E(\phi) = \tilde{E}(\tilde{\phi}) := \int_{\mathbb{R}^3} \left(\frac{1}{2}|\nabla\tilde{\phi}|^2 + V(P\tilde{\mathbf{x}})|\tilde{\phi}|^2 + \frac{\beta}{2}|\tilde{\phi}|^4 + |\boldsymbol{\Omega}|\tilde{\phi}^*L_z\tilde{\phi} \right) d\tilde{\mathbf{x}}. \tag{2.2}$$

Since the Household transform is a one-to-one map, the ground state existence is equivalent to the existence of minimizer to (2.2) under the same constraint in (1.6). Hereafter we shall focus on (2.2).

Using Young inequality, we have

$$\begin{aligned} \left| \int_{\mathbb{R}^3} |\boldsymbol{\Omega}|\tilde{\phi}^*L_z\tilde{\phi} d\tilde{\mathbf{x}} \right| &\leq \int_{\mathbb{R}^3} \left[|\boldsymbol{\Omega}|\tilde{x}\tilde{\phi}^*|\partial_{\tilde{y}}\tilde{\phi}| + |\boldsymbol{\Omega}|\tilde{y}\tilde{\phi}^*|\partial_{\tilde{x}}\tilde{\phi}| \right] d\tilde{\mathbf{x}} \\ &\leq \int_{\mathbb{R}^3} \left[\frac{|\boldsymbol{\Omega}|^2}{2}(\tilde{x}^2 + \tilde{y}^2)|\tilde{\phi}|^2 + \frac{1}{2}(|\partial_{\tilde{x}}\tilde{\phi}|^2 + |\partial_{\tilde{y}}\tilde{\phi}|^2) \right] d\tilde{\mathbf{x}}, \end{aligned}$$

and

$$\begin{aligned} \int_{\mathbb{R}^3} \left[\left(V(P\tilde{\mathbf{x}}) - \frac{|\boldsymbol{\Omega}|^2}{2}(\tilde{x}^2 + \tilde{y}^2) \right) |\tilde{\phi}|^2 + \frac{\beta}{2}|\tilde{\phi}|^4 \right] d\tilde{\mathbf{x}} &\leq \tilde{E}(\tilde{\phi}) \\ &\leq \int_{\mathbb{R}^3} \left[|\nabla\tilde{\phi}|^2 + \left(V(P\tilde{\mathbf{x}}) + \frac{|\boldsymbol{\Omega}|^2}{2}(\tilde{x}^2 + \tilde{y}^2) \right) |\tilde{\phi}|^2 + \frac{\beta}{2}|\tilde{\phi}|^4 \right] d\tilde{\mathbf{x}}. \end{aligned}$$

A lower bound is guaranteed if $U := V(P\tilde{\mathbf{x}}) - \frac{|\boldsymbol{\Omega}|^2}{2}(\tilde{x}^2 + \tilde{y}^2)$ is semi positive definite for $\tilde{\mathbf{x}} \in \mathbb{R}^3$. Expanding in full variables $\tilde{\mathbf{x}} = (\tilde{x}, \tilde{y}, \tilde{z})$ and rewriting it using matrix form, we have

$$\begin{aligned} U &= \frac{1}{2}\tilde{\mathbf{x}}^T P^T \begin{pmatrix} \gamma_x^2 & 0 & 0 \\ 0 & \gamma_y^2 & 0 \\ 0 & 0 & \gamma_z^2 \end{pmatrix} P\tilde{\mathbf{x}} - \frac{1}{2}\tilde{\mathbf{x}}^T \begin{pmatrix} |\boldsymbol{\Omega}|^2 & 0 & 0 \\ 0 & |\boldsymbol{\Omega}|^2 & 0 \\ 0 & 0 & 0 \end{pmatrix} \tilde{\mathbf{x}} \\ &= \frac{1}{2}\mathbf{x}^T \left[\begin{pmatrix} \gamma_x^2 & 0 & 0 \\ 0 & \gamma_y^2 & 0 \\ 0 & 0 & \gamma_z^2 \end{pmatrix} - |\boldsymbol{\Omega}|^2 P \begin{pmatrix} 1 & 0 & 0 \\ 0 & 1 & 0 \\ 0 & 0 & 0 \end{pmatrix} P^T \right] \mathbf{x} = \frac{1}{2}\mathbf{x}^T A \mathbf{x}. \end{aligned}$$

Therefore, we conclude that $\tilde{E}(\tilde{\phi})$ is positive if $\beta \geq 0$ and A is positive definite, so is $E(\phi)$. Moreover, we can prove that $E(\phi)$ is positive, coercive and weakly lower semi-continuous. Consequently, the existence of a minimum is established using the standard theory [34]. \square

3. Numerical method

Due to the external trapping potential, the wave function ϕ decays exponentially as $|\mathbf{x}| \rightarrow \infty$. Therefore, one can approximately truncate the wave function ϕ to a bounded domain $D := [L_x, R_x] \times [L_y, R_y] \times [L_z, R_z]$ with periodic boundary conditions. Based on this, in this section, we first discretize ϕ with standard pseudo-Fourier spectral method [9,12] and reformulate the constrained minimization problem (1.6) into its finite dimensional approximation. Then, a preconditioned Riemannian conjugate gradient method will be proposed to solve the resulted finite dimensional constrained minimization problem.

3.1. Discretization and the manifold geometry of the minimization problem

The mesh grids we used are chosen as $D_N = \{ \mathbf{x}_{jk\ell} := (x_j, y_k, z_\ell) := (L_x + jh_x, L_y + kh_y, L_z + \ell h_z), (j, k, \ell) \in O_N \}$ with mesh sizes $h_\nu = \frac{R_\nu - L_\nu}{N_\nu}$, N_ν ($\nu = x, y, z$) even numbers, $N := N_x N_y N_z$ and $O_N = \{ (j, k, \ell) \in \mathbb{N}^3 \mid 0 \leq j \leq N_x - 1, 0 \leq k \leq N_y - 1, 0 \leq \ell \leq N_z - 1 \}$. Moreover, we introduce the Fourier basis functions

$$W_{p_x p_y p_z}(\mathbf{x}) = \prod_{\nu=x,y,z} e^{i\mu_\nu^\nu (x-L_\nu)}, \quad p_\nu = -\frac{N_\nu}{2}, \dots, \frac{N_\nu}{2} - 1, \quad \nu = x, y, z,$$

with $\mu_{p_\nu}^\nu = \frac{2\pi p_\nu}{R_\nu - L_\nu}$ ($\nu = x, y, z$) the discrete Fourier frequencies. The Fourier pseudo-spectral approximation of the wave function ϕ as well as its derivatives at $\mathbf{x}_{jk\ell} \in D_N$ is given by

$$\begin{aligned} \phi(\mathbf{x}_{jk\ell}) &\approx \tilde{\phi}(\mathbf{x}_{jk\ell}) := \frac{1}{N} \sum_{p_x=-N_x/2}^{N_x/2-1} \sum_{p_y=-N_y/2}^{N_y/2-1} \sum_{p_z=-N_z/2}^{N_z/2-1} (\widehat{\phi})_{p_x p_y p_z} W_{p_x p_y p_z}(\mathbf{x}_{jk\ell}), \\ \partial_\nu \phi(\mathbf{x}_{jk\ell}) &\approx ([\partial_\nu] \tilde{\phi})_{jk\ell} := \frac{1}{N} \sum_{p_x=-N_x/2}^{N_x/2-1} \sum_{p_y=-N_y/2}^{N_y/2-1} \sum_{p_z=-N_z/2}^{N_z/2-1} (i\mu_{p_\nu}^\nu) (\widehat{\phi})_{p_x p_y p_z} W_{p_x p_y p_z}(\mathbf{x}_{jk\ell}), \quad \nu = x, y, z, \\ \partial_\nu^2 \phi(\mathbf{x}_{jk\ell}) &\approx ([\partial_\nu^2] \tilde{\phi})_{jk\ell} := -\frac{1}{N} \sum_{p_x=-N_x/2}^{N_x/2-1} \sum_{p_y=-N_y/2}^{N_y/2-1} \sum_{p_z=-N_z/2}^{N_z/2-1} (\mu_{p_\nu}^\nu)^2 (\widehat{\phi})_{p_x p_y p_z} W_{p_x p_y p_z}(\mathbf{x}_{jk\ell}), \quad \nu = x, y, z, \end{aligned}$$

where $(\widehat{\phi})_{p_x p_y p_z}$ are Fourier coefficients given by

$$(\widehat{\phi})_{p_x p_y p_z} = \sum_{j=0}^{N_x-1} \sum_{k=0}^{N_y-1} \sum_{\ell=0}^{N_z-1} \tilde{\phi}(\mathbf{x}_{jk\ell}) W_{p_x p_y p_z}^*(\mathbf{x}_{jk\ell}).$$

To discretize minimization problem (1.6), we also need the operators $y[[\partial_x]]$, $z[[\partial_x]]$, $x[[\partial_y]]$, $z[[\partial_y]]$, $x[[\partial_z]]$ and $y[[\partial_z]]$, which are applied to the approximation $\tilde{\phi}$ of ϕ , for $(j, k, \ell) \in O_N$,

$$\begin{aligned} (x\partial_\nu \phi)(\mathbf{x}_{jk\ell}) &\approx (x[[\partial_\nu]] \tilde{\phi})_{jk\ell} := x_j ([\partial_\nu] \tilde{\phi})_{jk\ell}, \quad \nu = y, z, \\ (y\partial_\nu \phi)(\mathbf{x}_{jk\ell}) &\approx (y[[\partial_\nu]] \tilde{\phi})_{jk\ell} := y_k ([\partial_\nu] \tilde{\phi})_{jk\ell}, \quad \nu = x, z, \\ (z\partial_\nu \phi)(\mathbf{x}_{jk\ell}) &\approx (z[[\partial_\nu]] \tilde{\phi})_{jk\ell} := z_\ell ([\partial_\nu] \tilde{\phi})_{jk\ell}, \quad \nu = x, y. \end{aligned}$$

Denote $g_{jk\ell} := g(\mathbf{x}_{jk\ell})$ as the value of an abstract function $g(\mathbf{x})$ (g represents $\phi, \phi^2, |\phi|^2, V$, etc) at $\mathbf{x}_{jk\ell} \in D_N$ and let g be the vector with elements $g_{jk\ell}$. Together with the operators

$$[[\Delta]] := [[\partial_x^2]] + [[\partial_y^2]] + [[\partial_z^2]], \quad [[L_x]] := -i(y[[\partial_z]] - z[[\partial_y]]), \quad [[L_y]] := -i(z[[\partial_x]] - x[[\partial_z]]), \quad [[L_z]] := -i(x[[\partial_y]] - y[[\partial_x]]),$$

we discretize the energy functional $E(\phi)$ as

$$E(\phi) \approx \mathcal{E}(\phi) := \left\langle -\frac{1}{2} [[\Delta]] \phi + V \odot \phi + \frac{\beta}{2} (|\phi|^2) \odot \phi - (\omega_x [[L_x]] \phi + \omega_y [[L_y]] \phi + \omega_z [[L_z]] \phi), \phi \right\rangle,$$

and the minimization problem (1.6) is then discretized into the finite dimensional minimization problem

$$\phi_g = \underset{\phi \in S}{\operatorname{argmin}} \mathcal{E}(\phi), \quad \text{with} \quad S := \{\phi \in \mathbb{C}^N \mid \|\phi\|^2 = 1\}. \tag{3.1}$$

Here, \odot denotes the Hadamard product, $\langle \cdot, \cdot \rangle$ and $\|\cdot\|$ are respectively the (scaled) Euclidean metric and its induced norm defined by

$$\langle U, V \rangle := \operatorname{Re} \left(h_x h_y h_z \sum_{j=0}^{N_x-1} \sum_{k=0}^{N_y-1} \sum_{\ell=0}^{N_z-1} U_{jk\ell} V_{jk\ell}^* \right), \quad \|U\| = \sqrt{\langle U, U \rangle}, \quad U, V \in \mathbb{C}^N, \tag{3.2}$$

with $\operatorname{Re}(\cdot)$ representing the real part. The difficulties of classical methods based on gradient-type flows to solve (3.1) come from the proper treatment of the constraint in S . However, S can be viewed as the spherical manifold and thus leads problem (3.1) to be a minimization problem on Riemannian manifold. Hence, problem (3.1) can be treated as an *unconstrained* optimization problem on the spherical manifold S , and efficient preconditioned Riemannian conjugate gradient (pRCG) method [2] could be applied to solve it. We state the geometry structure that the pRCG method (stated later in subsection 3.2) relies on thereafter.

The Riemannian metric we use is the Euclidean metric (3.2). Recall that the Riemannian manifold of the optimization problem (3.1) reads as $S = \{\phi \in \mathbb{C}^N \mid \|\phi\|^2 = 1\}$. The tangent space of S at $\phi \in S$ is

$$\mathcal{T}_\phi S := \{u \in \mathbb{C}^N \mid \langle \phi, u \rangle = 0\}, \tag{3.3}$$

and the orthogonal projection operator M_ϕ onto this space is given by

$$M_\phi u := u - \langle u, \phi \rangle \phi, \quad \forall u \in \mathbb{C}^N. \tag{3.4}$$

For energy functional $\mathcal{E}(\phi)$, by a direct calculation via Gâteaux differential, one obtains its Euclidean gradient $\nabla \mathcal{E}(\phi)$ and the action of its Euclidean Hessian $\nabla^2 \mathcal{E}$ at ϕ on u

$$\nabla \mathcal{E}(\phi) = 2\mathcal{H}_\phi \phi, \quad \nabla^2 \mathcal{E}(\phi)[u] = 2\mathcal{H}_\phi u + 2\beta \phi^2 \odot u^* + 2\beta |\phi|^2 \odot u,$$

$$\text{with } \mathcal{H}_\phi u = \left(-\frac{1}{2} [\Delta] - \omega_x [L_x] - \omega_y [L_y] - \omega_z [L_z] \right) u + (V + \beta |\phi|^2) \odot u, \quad \forall \phi, u \in \mathbb{C}^N.$$

The Riemannian gradient of $\mathcal{E}(\phi)$ at ϕ and the action of the Riemannian Hessian operator of $\mathcal{E}(\phi)$ at ϕ along $u \in \mathcal{T}_\phi S$, denoted respectively by $\text{grad } \mathcal{E}(\phi)$ and $\text{Hess } \mathcal{E}(\phi)[u]$, can be explicitly computed as:

$$\text{grad } \mathcal{E}(\phi) = M_\phi (\nabla \mathcal{E}(\phi)) = \nabla \mathcal{E}(\phi) - \langle \nabla \mathcal{E}(\phi), \phi \rangle \phi, \quad \forall \phi \in S, \tag{3.5}$$

$$\text{Hess } \mathcal{E}(\phi)[u] = M_\phi (\nabla^2 \mathcal{E}(\phi)[u]) - \langle \nabla \mathcal{E}(\phi), \phi \rangle u, \quad \forall u \in \mathcal{T}_\phi S. \tag{3.6}$$

The first-order and second-order necessary optimality conditions [2] for the optimization problem (3.1) state that at a minimum $\phi \in S$, $\text{grad } \mathcal{E}(\phi) = 0$ and $\langle \text{Hess } \mathcal{E}(\phi)[u], u \rangle \geq 0$. This immediately implies

$$\mathcal{H}_\phi \phi = \lambda_\phi \phi, \quad \frac{1}{2} \nabla^2 \mathcal{E}(\phi)[u, u] - \lambda_\phi \|u\|_2^2 \geq 0, \quad \forall u \in \mathcal{T}_\phi S. \tag{3.7}$$

Here, $\lambda_\phi = \langle \mathcal{H}_\phi \phi, \phi \rangle$ and $\nabla^2 \mathcal{E}(\phi)[u, u] := \langle \nabla^2 \mathcal{E}(\phi)[u], u \rangle$. The first equation is indeed the Euler-Lagrange equation associated with our problem (3.1), and λ_ϕ is the Lagrange multiplier which is also known as the chemical potential [9,11].

3.2. A preconditioned Riemannian conjugate gradient method

Algorithms on Riemannian manifold, such as the analogues of steepest descent and nonlinear conjugate gradient methods in Euclidean cases [29], have been extensively developed [2]. It was also observed that usually the Riemannian conjugate gradient algorithm converges faster than other simple gradient-type algorithms [2,9,35]. Therefore, here we propose a Riemannian conjugate gradient method with a suitable preconditioner to solve the Riemannian optimization problem (3.1). To this end, in addition to the definitions of tangent space, projection and Riemannian gradient/Hessian operator given in (3.3)-(3.6), we also need a *retraction* map to enforce the search direction so that the resulted updates stay on the manifold S and a *vector transport* map to move vectors in two different tangent spaces such that they are additive. For the spherical manifold S , these two maps are readily given explicitly [2,9].

Denote $\mathcal{T}S := \bigcup_{\phi \in S} \mathcal{T}_\phi S$ as the tangent bundle of S . Then, for $\forall \phi \in S$, the retraction $\mathcal{R}_\phi : \mathcal{T}_\phi S \rightarrow S$ reads as

$$\mathcal{R}_\phi(\alpha v) := \cos(\|\alpha v\|) \phi + \frac{\sin(\|\alpha v\|)}{\|\alpha v\|} v, \quad \forall v \in \mathcal{T}_\phi S, \quad \alpha \geq 0. \tag{3.8}$$

While the vector transport $T : \mathcal{T}S \times \mathcal{T}S \rightarrow \mathcal{T}S : (u, v) \rightarrow T_u(v)$ using Riemannian submanifold structure reads as

$$T_{u_\phi}(v_\phi) := M_{\mathcal{R}_\phi(u_\phi)} v_\phi = v_\phi - \langle v_\phi, \mathcal{R}_\phi(u_\phi) \rangle \mathcal{R}_\phi(u_\phi), \quad \forall u_\phi \in \mathcal{T}_\phi S, v_\phi \in \mathcal{T}_\phi S, \tag{3.9}$$

which maps/moves the vector in tangent space $\mathcal{T}_\phi S$ onto $\mathcal{T}_{\mathcal{R}_\phi(u_\phi)} S$ along the manifold S by the vector u_ϕ , so that algebraic operations can be performed on vectors belonging to $\mathcal{T}_\phi S$ and $\mathcal{T}_{\mathcal{R}_\phi(u_\phi)} S$.

With the concepts defined above (cf. (3.3)-(3.9)), the pRCG algorithm for the minimization of $\mathcal{E}(\phi)$ on S (3.1) is stated as follows: given $\phi_0 \in S$, update

$$\phi_{n+1} = \mathcal{R}_{\phi_n}(\alpha_n d_n) = \cos(\|\alpha_n d_n\|) \phi_n + \frac{\sin(\|\alpha_n d_n\|)}{\|\alpha_n d_n\|} d_n, \quad n = 0, 1, \dots, \tag{3.10}$$

where α_n is the step size to be computed later, and d_n is the search direction at ϕ_n chosen as

$$d_0 = M_{\phi_0}(-\mathcal{P} \text{grad } \mathcal{E}(\phi_0)), \quad d_n = M_{\phi_n}(-\mathcal{P} \text{grad } \mathcal{E}(\phi_n)) + \beta_n T_{\alpha_{n-1} d_{n-1}}(d_{n-1}), \quad n \geq 1. \tag{3.11}$$

Here, \mathcal{P} is a symmetric positive definite preconditioner to be determined, and β_n is the Polak-Ribière momentum term which is typically computed via [2]

$$\beta_n = \max(\beta_n^{PR}, 0), \quad \text{with } \beta_n^{PR} = \frac{\langle \text{grad } \mathcal{E}(\phi_n) - T_{\alpha_{n-1} d_{n-1}}(\text{grad } \mathcal{E}(\phi_{n-1})), M_{\phi_n}(\mathcal{P} \text{grad } \mathcal{E}(\phi_n)) \rangle}{\langle \text{grad } \mathcal{E}(\phi_{n-1}), M_{\phi_{n-1}}(\mathcal{P} \text{grad } \mathcal{E}(\phi_{n-1})) \rangle}. \tag{3.12}$$

We use $\beta_n = \max(\beta_n^{PR}, 0)$, which is equivalent to restarting the pRCG method (simply using a steepest descent step) when $\beta_n^{PR} \leq 0$ and is a standard choice in nonlinear CG methods [9,35].

Similar to the nonlinear CG method in the Euclidean setting [35], proper choice of the stepsize α_n is important for the performance of pRCG method. A standard approach is to perform linesearch methods to the one-dimensional nonlinear minimization problem

$$\alpha_n = \underset{\alpha > 0}{\text{argmin}} \mathcal{E}(\mathcal{R}_{\phi_n}(\alpha d_n)), \tag{3.13}$$

which could be expensive and time consuming. Alternatively, now that the retraction (3.8) is second order, we could propose a simple and cheap approach based on the Taylor expansion of $F(\alpha) := \mathcal{E}(\mathcal{R}_{\phi_n}(\alpha d_n))$ as follows

$$F(\alpha) = \mathcal{E}(\phi_n) + \alpha \langle \text{grad } \mathcal{E}(\phi_n), d_n \rangle + \frac{\alpha^2}{2} \langle \text{Hess } \mathcal{E}(\phi_n)[d_n], d_n \rangle + O(\alpha^3). \tag{3.14}$$

When $\beta_n = 0$ in (3.12) (i.e. the pRCG method reduces to steepest descent method), the first-order variation

$$\left\langle \text{grad}\mathcal{E}(\phi_n), d_n \right\rangle = -\left\langle \text{grad}\mathcal{E}(\phi_n), \mathcal{P} \text{grad}\mathcal{E}(\phi_n) \right\rangle < 0 \quad (3.15)$$

is guaranteed since the preconditioner \mathcal{P} is positive definite. This ensures that the energy is diminishing when α is small enough. In addition, due to the second-order optimality condition (3.7), the second-order variation

$$\left\langle \text{Hess}\mathcal{E}(\phi_n)[d_n], d_n \right\rangle > 0 \quad (3.16)$$

is also ensured when ϕ_n is close enough to a minimizer. As such, a candidate to approximate step size α_n in (3.13) can be obtained by minimizing the second order approximation of $\mathcal{F}(\alpha)$ (3.14) w.r.t. α , which yields

$$\alpha_n^{opt} := -\left\langle \text{grad}\mathcal{E}(\phi_n), d_n \right\rangle / \left\langle \text{Hess}\mathcal{E}(\phi_n)[d_n], d_n \right\rangle > 0. \quad (3.17)$$

In the practical computation of pRCG, when $\beta_n \neq 0$, d_n may not be a descent direction and ϕ_n may be far from a minimizer. Hence, with $\alpha_n = \alpha_n^{opt}$ or even a small stepsize, the energy dissipation is not guaranteed at each iteration. To enforce energy decrease, our strategy is as follows: First, check the validity of (3.15) and (3.16). If either of them is invalid, we set $\beta_n = 0$ and choose a small positive number as the trail step size of α_n . Backtrack this trail step size until the energy is decreased and accept the resulting step size as α_n . Secondly, if both (3.15) & (3.16) hold true, we choose

$$\alpha_n = \alpha_n^{opt}. \quad (3.18)$$

To close, we now consider the question of building preconditioners \mathcal{P} for the presented pRCG algorithm above. A preconditioner \mathcal{P} in the pRCG method (3.11)-(3.12) at ϕ_n should be a positive-definite linear operator that approximates the inverse of the Riemannian Hessian $\text{Hess}\mathcal{E}(\phi_n)$. Recalling the expression of $\text{Hess}\mathcal{E}(\phi_n)$ in (3.6), we combine parts of it whose inverse can be easily computed to form a preconditioner:

$$\mathcal{P} = \mathcal{P}_V^{1/2} \mathcal{P}_\Delta \mathcal{P}_V^{1/2}, \quad \text{with } \mathcal{P}_\Delta = (\alpha_\Delta - \llbracket \Delta \rrbracket / 2)^{-1}, \quad \mathcal{P}_V = (\alpha_V + V + \beta |\phi_n|^2)^{-1}. \quad (3.19)$$

Here, α_Δ and α_V are positive constants chosen such that \mathcal{P}_Δ and \mathcal{P}_V are invertible, and here we choose

$$\alpha_\Delta = \alpha_V := \left\langle -\frac{1}{2} \llbracket \Delta \rrbracket \phi_n + V \odot \phi_n + \beta (|\phi_n|^2) \odot \phi_n, \phi_n \right\rangle.$$

The pRCG algorithm is summarized in Algorithm 1.

Algorithm 1: The preconditioned Riemannian conjugate gradient (pRCG) method.

Input initial data ϕ_0 , stopping criteria ε and trial stepsize $\alpha_{trail} \in (0, 1)$.

Compute $d_0 = M_{\phi_0}(-\mathcal{P} \text{grad} \mathcal{E}(\phi_0))$.

Set $n = 0$ and $\varepsilon_{err}^0 = 1$.

while not converged (i.e. $\varepsilon_{err}^n > \varepsilon$) **do**

Step 1: Perform linesearch backtracking methods to update

$$\alpha_n := \underset{\alpha > 0}{\text{argmin}} \mathcal{E}(\mathcal{R}_{\phi_n}(\alpha d_n)),$$

where the initial step size α_n^0 is chosen as

$$\alpha_n^0 = \max(\alpha_n^{opt}, \alpha_{trail}).$$

Step 2: Update $\phi_{n+1} = \mathcal{R}_{\phi_n}(\alpha_n d_n)$.

Step 3: If either (3.15) or (3.16) is invalid, set $\beta_{n+1} = 0$;

otherwise, compute β_{n+1}^{PR} via (3.12) and set $\beta_{n+1} = \max(\beta_{n+1}^{PR}, 0)$.

Step 4: Update search direction d_{n+1} via:

$$d_{n+1} = M_{\phi_{n+1}}(-\mathcal{P} \text{grad} \mathcal{E}(\phi_{n+1})) + \beta_{n+1} T_{\alpha_n d_n}(d_n).$$

Step 5: Check the error: $\varepsilon_{err}^n := \|\phi_{n+1} - \phi_n\|_\infty$.

Step 6: Update step: $n = n + 1$.

end

4. Numerical results

In this section, we first test the accuracy and efficiency of the pRCG method. Then, we apply the pRCG method to investigate the GS patterns of arbitrary-angle rotating BEC under different settings, especially in the case when the rotation axis is not parallel to the elongated direction of the condensates. To this end, unless specified, the computational domain, the mesh size in each direction and the stopping criteria in Algorithm 1 are respectively chosen as $D = [-16, 16]^3$, $h_x = h_y = h_z = \frac{1}{8}$ and $\varepsilon = 10^{-12}$. In the following

numerical tests, we consider three types of trapping potential $V(\mathbf{x})$: the harmonic potential (1.2), the harmonic-plus-quartic potential [9,20]

$$V_{\text{hq}}(\mathbf{x}) := V_{\text{har}}(\mathbf{x}) - \alpha(x^2 + y^2) + \kappa(c_1x^2 + c_2y^2 + c_3z^2)^2/4, \tag{4.1}$$

and the toroidal potential (4.2) with $V_0 > 0$, which uses a blue-detuned laser beam to make a repulsive potential barrier in the middle of a harmonic trap [32]

$$V_{\text{tor}}(\mathbf{x}) := V_{\text{har}}(\mathbf{x}) + V_0e^{-a^2|\mathbf{x}|^2}. \tag{4.2}$$

Moreover, to obtain GS, we first utilize the pRCG algorithm with the following twelve frequently used initial data to get stationary states. The resulted one with the lowest energy is then regarded as the GS:

$$\begin{aligned} (a) \phi_a(\mathbf{x}) &= \frac{1}{\sqrt[4]{\pi^3}}e^{-\frac{|\mathbf{x}|^2}{2}}, & (b) \phi_b(\mathbf{x}) &= \frac{(x+iy)\phi_a(\mathbf{x})}{\|(x+iy)\phi_a(\mathbf{x})\|}, & (c) \phi_c(\mathbf{x}) &= \frac{(\phi_a(\mathbf{x})+\phi_b(\mathbf{x}))}{\|(\phi_a(\mathbf{x})+\phi_b(\mathbf{x}))\|}, \\ (d) \phi_d(\mathbf{x}) &= \frac{(1-|\Omega|)\phi_a(\mathbf{x})+|\Omega|\phi_b(\mathbf{x})}{\|(1-|\Omega|)\phi_a(\mathbf{x})+|\Omega|\phi_b(\mathbf{x})\|}, & (\bar{b}) \phi_{\bar{b}}(\mathbf{x}) &= \phi_b^*(\mathbf{x}), & (\bar{c}) \phi_{\bar{c}}(\mathbf{x}) &= \phi_c^*(\mathbf{x}), \\ (e) \phi_e(\mathbf{x}) &= \frac{|\Omega|\phi_a(\mathbf{x})+(1-|\Omega|)\phi_b(\mathbf{x})}{\| |\Omega|\phi_a(\mathbf{x})+(1-|\Omega|)\phi_b(\mathbf{x}) \|}, & (f) \phi_f(\mathbf{x}) &= \frac{\phi_g^{\text{TF}}(\mathbf{x})}{\|\phi_g^{\text{TF}}(\mathbf{x})\|}, & (\bar{d}) \phi_{\bar{d}}(\mathbf{x}) &= \phi_d^*(\mathbf{x}), \\ (\check{f}) \phi_{\check{f}}(\mathbf{x}) &= \frac{(1-|\Omega|)\phi_g^{\text{TF}}(\mathbf{x})+|\Omega|(x-iy)\phi_g^{\text{TF}}(\mathbf{x})}{\|(1-|\Omega|)\phi_g^{\text{TF}}(\mathbf{x})+|\Omega|(x-iy)\phi_g^{\text{TF}}(\mathbf{x})\|}, & (\bar{e}) \phi_{\bar{e}}(\mathbf{x}) &= \phi_e^*(\mathbf{x}), & (\bar{f}) \phi_{\bar{f}}(\mathbf{x}) &= \phi_f^*(\mathbf{x}). \end{aligned}$$

Here, $\Omega = (\omega_x, \omega_y, \omega_z)^T = \sqrt{\omega_x^2 + \omega_y^2 + \omega_z^2} \mathbf{n} =: |\Omega| \mathbf{n}$ with $\mathbf{n} = (n_1, n_2, n_3)^T$, and

$$\phi_g^{\text{TF}} = \begin{cases} \sqrt{(\mu_g^{\text{TF}} - V(\mathbf{x}))/\beta}, & V(\mathbf{x}) < \mu_g^{\text{TF}}, \\ 0, & \text{otherwise,} \end{cases} \quad \mu_g^{\text{TF}} = \frac{1}{2} \left(\frac{15\beta\gamma_x\gamma_y\gamma_z}{4\pi} \right)^{2/5},$$

is the Thomas Fermi approximation of the GS [8,11]. For simplicity, we denote a rotation orientation that will be frequently used in the following numerical examples

$$\mathbf{n}_0 := \mathbf{n} = \left(\frac{\sqrt{3}}{3}, \frac{\sqrt{3}}{3}, \frac{\sqrt{3}}{3} \right)^T.$$

The pRCG algorithm was implemented in Matlab (2022) and runs on a 3.00GH Intel(R) Xeon(R) Gold 6136R CPU with 36 MB cache in Ubuntu GNU/Linux.

4.1. Accuracy and efficiency test

Similar as in the nonrotating BEC [11], if potential $V(\mathbf{x})$ is taken as the harmonic one (1.2), the energies of the ground state ϕ_g of the arbitrary-angle rotating BEC satisfy the following virial identity

$$I(\phi_g) := 2E_{\text{kin}}(\phi_g) - 2E_{\text{pot}}(\phi_g) + 3E_{\text{int}}(\phi_g) = 0, \tag{4.3}$$

with

$$E_{\text{kin}}(\phi_g) = \frac{1}{2} \int_{\mathbb{R}^3} |\nabla \phi_g|^2 d\mathbf{x}, \quad E_{\text{pot}}(\phi_g) = \int_{\mathbb{R}^3} V(\mathbf{x})|\phi_g|^2 d\mathbf{x}, \quad E_{\text{int}}(\phi_g) = \frac{\beta}{2} \int_{\mathbb{R}^3} |\phi_g|^4 d\mathbf{x}.$$

This identity, together with the first-order optimality condition (3.7), could be used as the benchmark to check the accuracy of the pRCG algorithm. For simplicity, we denote I_g as the pseudo-spectral discretization of $I(\phi_g)$, $r_g := \mathcal{H}_{\phi_g} \phi_g - \lambda_{\phi_g} \phi_g$ as the residual associated with the first-order optimality condition (3.7) and $\mathcal{E}_g := \mathcal{E}(\phi_g)$ as the ground state energy.

Example 4.1. In this example, we test the accuracy and efficiency of pRCG method. To this end, we fix $\beta = 100$, rotation frequency $\Omega = |\Omega| \mathbf{n}_0$ with varied $|\Omega| = 0.2, 0.4, 0.6, 0.8$. Meanwhile, we take potential $V(\mathbf{x})$ as the harmonic potential $V_{\text{har}}(\mathbf{x})$ (1.2) and consider the following trapping frequencies:

Case 1. Isotropic trapping: $\gamma_x = \gamma_y = \gamma_z = 1$. **Case 2.** Anisotropic trapping: $\gamma_x = 1, \gamma_y = 2, \gamma_z = 3$.

Table 1 lists the total energy \mathcal{E}_g , virial $|I_g|$ and residual $\|r_g\|_\infty$ of the converged GS $\phi_g(\mathbf{x})$ for these two cases with different $|\Omega|$. The corresponding initial data and CPU time that the pRCG algorithm used to get $\phi_g(\mathbf{x})$ are also listed in the same table. In addition, Figs. 1 & 2 show the evolution of the total energy $\mathcal{E}^n := \mathcal{E}(\phi^n)$ versus iteration step n and the isosurface plots of $|\phi_g(\mathbf{x})|^2 = 10^{-3}$ for different $|\Omega|$. From these figures, tables and additional numerical results not shown here for brevity, we can see that: (i) The total energy \mathcal{E} is diminishing during iteration (cf. Fig. 1). And the pRCG algorithm is capable of computing GS of BEC with arbitrary-angle rotation accurately and efficiently (cf. Table 1 and Fig. 1). (ii) For the case of isotropic trapping potential, the density of BEC is in

Table 1

Total energy \mathcal{E}_g , virial $|I_g|$ and residual $\|r_g\|_\infty$ of the converged GS $\phi_g(\mathbf{x})$, as well as the initial data ϕ_0 and CPU time the pRCG used to converge to GS $\phi_g(\mathbf{x})$ in **Example 4.1**.

	$ \Omega $	ϕ_0	\mathcal{E}_g	$ I_g $	$\ r_g\ _\infty$	CPU(s)
Case 1 (isotropic)	0.2	(a)	2.8679204104619	1.3875E-11	9.7193E-11	153
	0.4	(b)	2.8679204104619	5.1794E-12	4.0507E-11	575
	0.6	(\bar{e})	2.8679204104619	4.4316E-12	5.1730E-11	97
	0.8	(\check{f})	2.6823300688629	3.0131E-12	1.0004E-10	1464
Case 2 (anisotropic)	0.2	(f)	5.8933514312585	5.4774E-12	1.1848E-10	115
	0.4	(f)	5.8493208273254	8.1712E-14	4.6788E-11	215
	0.6	(\bar{d})	5.7614222409060	3.2134E-12	9.2939E-11	314
	0.8	(b)	5.5924954863850	8.5354E-13	1.2495E-10	424

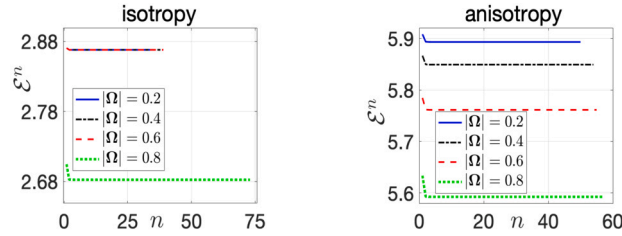


Fig. 1. Evolution of the energy $\mathcal{E}^n := \mathcal{E}(\phi_n)$ vs. the iteration step n in **Example 4.1**.

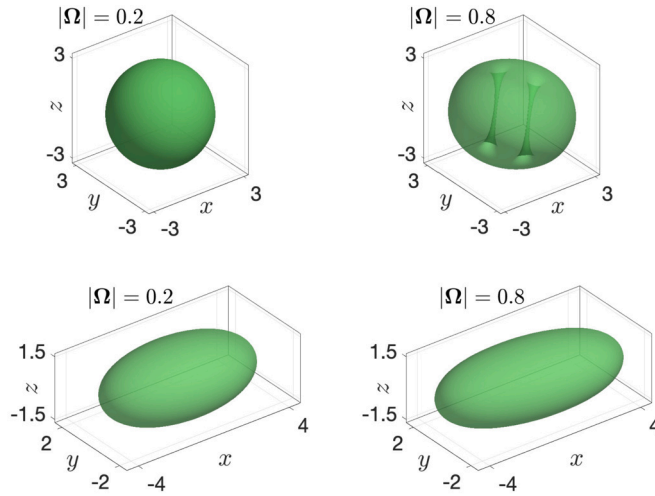


Fig. 2. Isosurface plots of $|\phi_g(\mathbf{x})|^2 = 10^{-3}$ with different $|\Omega|$ for **Case 1** (upper) and **Case 2** (lower) in **Example 4.1**.

spherical shape (cf. upper row in Fig. 2). The GS energy of BEC without vortex is the same. When $|\Omega|$ is large enough, symmetric-breaking occurs and vortices are brought into the condensate. The GS energy then decreases as $|\Omega|$ increases (cf. Table 1). (iii) For the case of anisotropic trapping potential, the density profile of BEC is elongated along the force field induced by the potential, which leads to ellipsoidal-shaped condensates (cf. lower row in Fig. 2). The larger the $|\Omega|$, the longer the condensate will be elongated (due to the centrifugal force induced by the rotation), and the lower the total energy of the related ground state (cf. Table 1). Moreover, the critical value of $|\Omega|$ to create the first vortex is larger than those in an isotropic trap.

4.2. New vortex structure in anisotropic BEC

Bent vortices [24,25], a remarkable phenomenon that inspires the exploration of vortex lines, can be observed in an elongated rotating BEC with strong local interaction. In this subsection, we apply pRCG algorithm to investigate the vortex structures in GS of anisotropic BEC, especially the bent vortices and their relations w.r.t. the angle between the rotation axis and the elongated direction of the condensate. To this end, we choose potential $V(\mathbf{x})$ as the harmonic potential $V_{\text{har}}(\mathbf{x})$ (1.2) with $\gamma_y = \gamma_z = 1$ and $\gamma_x < 1$, i.e. the condensate is elongated along x -axis.

Example 4.2. Here, we set $\Omega = (\omega_x, \omega_y, 0)^T$ and consider the following three cases:

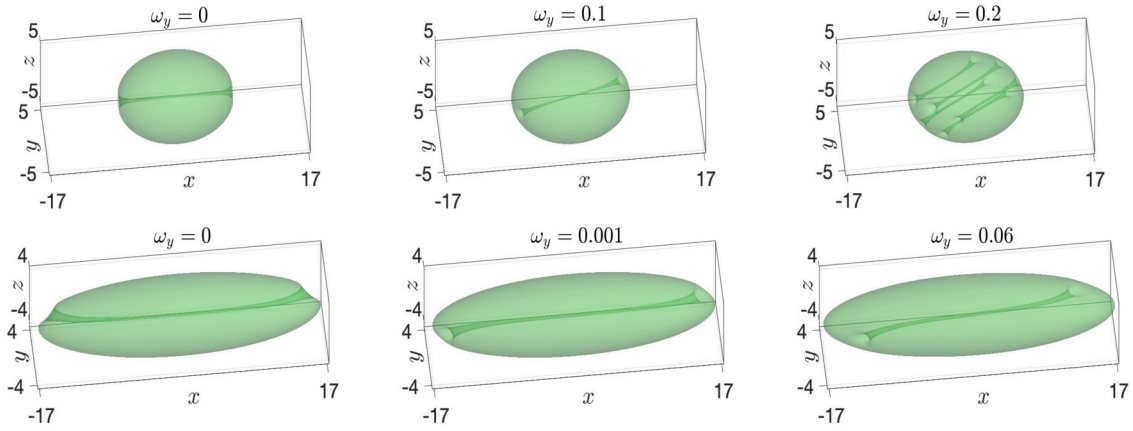


Fig. 3. Isosurface of $|\phi_g(\mathbf{x})|^2 = 3 \times 10^{-4}$ for Case 1(upper) and Case 2 in Example 4.2.

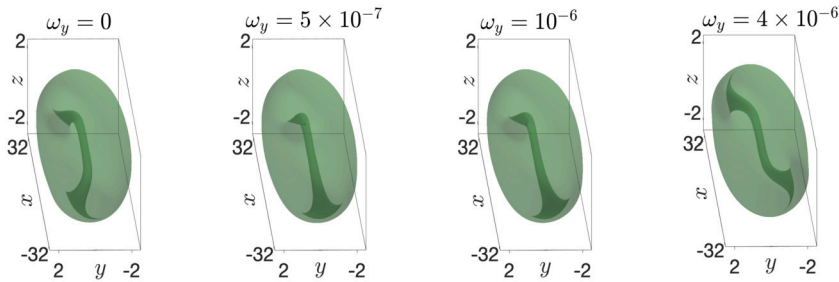


Fig. 4. Isosurface of $|\phi_g(\mathbf{x})|^2 = 3 \times 10^{-4}$ for Case 3 in Example 4.2.

Table 2
Total energy \mathcal{E}_g , virial $|I_g|$ and residual $\|r_g\|_\infty$ of the converged GS $\phi_g(\mathbf{x})$ in Example 4.2.

	γ_x	ω_y	ϕ_0	\mathcal{E}_g	$ I_g $	$\ r_g\ _\infty$
Case 1	0.7	0	(b)	12.624833871315142	6.714629E-13	7.177332E-11
	0.7	0.1	(b)	12.569389786882745	1.293543E-11	3.290184E-11
	0.7	0.2	(f)	12.376530806382885	1.509903E-13	5.736563E-11
Case 2	0.25	0	(d)	8.479507974932206	1.778133E-12	4.860156E-11
	0.25	0.001	(d)	8.479397993330114	3.552714E-13	3.341535E-11
	0.25	0.06	(b)	8.379219530221569	1.723066E-12	5.040286E-11
Case 3	0.05	0	(f)	2.129112063451595	3.252953E-13	8.347278E-11
	0.05	5×10^{-7}	(f)	2.129112055891263	3.085310E-12	7.835594E-11
	0.05	10^{-6}	(f)	2.129112033209414	1.760148E-12	9.062290E-11
	0.05	4×10^{-6}	(c)	2.129111670223471	8.579804E-13	6.528560E-11

Case 1. Fix $\beta = 9000$, $\gamma_x = 0.7$, $\omega_x = 0.35$ and vary ω_y among 0, 0.1, 0.2.

Case 2. Fix $\beta = 9000$, $\gamma_x = 0.25$, $\omega_x = 0.35$ and vary ω_y among 0, 0.001, 0.06.

Case 3. Fix $\beta = 1000$, $\gamma_x = 0.05$, $\omega_x = 0.75$ and vary ω_y among 0, 5×10^{-7} , 10^{-6} and 4×10^{-6} .

We take computational domain $D = [-40, 40] \times [-10, 10]^2$ with mesh size $h_x = h_y = h_z = \frac{1}{12}$ for Case 1-2, and take $D = [-50, 50] \times [-8, 8]^2$ with $h_x = h_y = h_z = \frac{1}{8}$ for Case 3. Table 2 lists the total energy \mathcal{E}_g , virial $|I_g|$ and residual $\|r_g\|_\infty$ of the converged GS $\phi_g(\mathbf{x})$, while Figs. 3–4 illustrate the isosurface plots of $|\phi_g(\mathbf{x})|^2 = 3 \times 10^{-4}$ for the three cases. From these figures and additional numerical results not shown here for brevity, we can see that: (i) For a slow-rotating system in an isotropic/mild-anisotropic trapping potential and/or highly fast-rotating system, the vortex line is straight and aligned parallel to the rotation axis (cf. upper row in Fig. 3 and Figs. 5–8). (ii) Bent vortices occur only in strongly anisotropic trapping with slow rotation (i.e. γ_x becomes smaller in this example). When the rotation axis is parallel to the elongated direction, straight vortex lines will be bent into U-shaped curves (cf. the first column in Fig. 3 & Fig. 4). This phenomenon is in consistent with the observation in [24]. (iii) In addition to (ii), as the rotation axis shifts away from the elongated direction (i.e. ω_y becomes larger in this example), U-shaped vortex lines will gradually transform into planar S-shaped vortex lines (cf. Fig. 4).

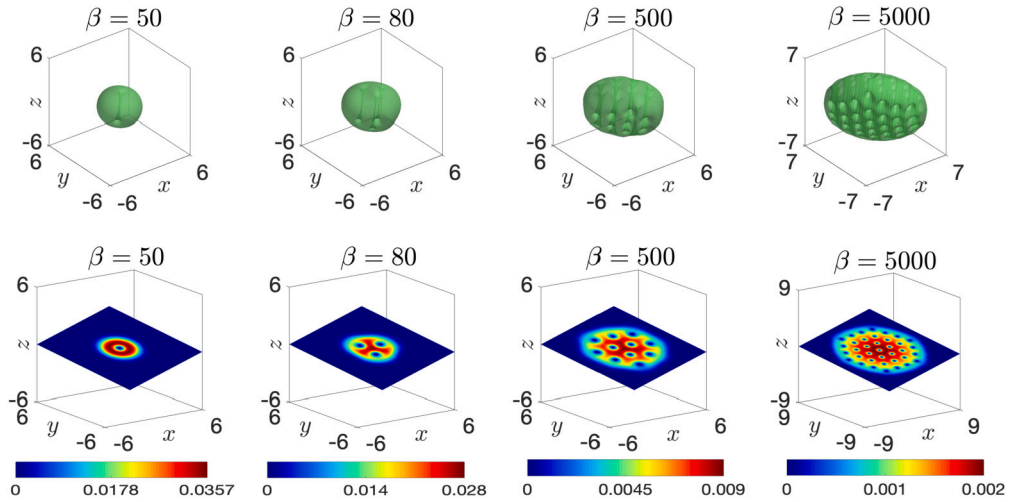


Fig. 5. Isosurface of $|\phi_g(x)|^2 = 0.02$ (upper first figure) & $|\phi_g(x)|^2 = 5 \times 10^{-4}$ (upper right three figures) and slice of $|\phi_g(x)|^2$ perpendicular to the rotation axis (lower) for Case 1 of Example 4.3.

4.3. GS patterns under different model parameters

In this subsection, we apply the pRCG algorithm to investigate the impacts of trapping potential $V(x)$, nonlinearity strength β , the amplitude $|\Omega|$ and orientation of rotation \mathbf{n} on the structure of GS. Unless specified, hereafter we fix $\gamma_x = \gamma_y = \gamma_z = 1$ in all the three type potentials (1.2), (4.1) & (4.2).

Example 4.3. Here, we choose potential $V(x)$ as the harmonic potential and consider the following cases:

- Case 1.** Set $|\Omega| = 0.85$, $\mathbf{n} = \mathbf{n}_0$ and vary β among 50, 80, 500, 5000.
- Case 2.** Set $\beta = 100$, $\mathbf{n} = \mathbf{n}_0$ and vary $|\Omega|$ among 0.5, 0.73, 0.81, 0.86.
- Case 3.** Set $\beta = 100$, $|\Omega| = 0.85$ and vary \mathbf{n} among \mathbf{n}_0 , $(1, 0, 0)^T$, $(0, 1, 0)^T$, $(0, 0, 1)^T$.

Figs. 5–7 illustrate the isosurface plots of $|\phi_g(x)|^2 = 5 \times 10^{-4}$ for Case 1 while $|\phi_g(x)|^2 = 10^{-3}$ for Case 2 & for Case 3 as well as the corresponding slice plots of $|\phi_g(x)|^2$ perpendicular to rotation axis \mathbf{n} . From these figures and additional numerical results not shown here for brevity, we can see that: (i) For fast rotation, i.e. $|\Omega|$ is large, the vortex line is straight (cf. Figs. 5–7). Moreover, the number of vortex lines is independent of the orientation of rotation \mathbf{n} if the trapping potential is isotropic (cf. Fig. 7). (ii) For a fixed rotation frequency Ω , number of vortex lines increases as the nonlinear interaction strength β getting larger (cf. Fig. 5). Moreover, for fixed orientation of rotation \mathbf{n} and nonlinear interaction strength β , number of vortex lines also increases as $|\Omega|$ increases (cf. Fig. 6).

Example 4.4. Here, we choose potential $V(x)$ as the harmonic-plus-quartic trapping potential $V_{\text{hq}}(x)$ (4.1) with $c_2 = 1$, and consider the following cases:

- Case 1.** Set $\beta = 10000$, choose $\gamma_z = \sqrt{2}$, $\alpha = 0.4$, $\kappa = 0.3$, $c_1 = 1$, $c_3 = 0$ and $\mathbf{n} = (0, 0, 1)^T$. In such a setting, both the elongated direction of the condensate and the rotation axis are parallel to z -axis. We then study the impact of rotation amplitude on the GS by varying $|\Omega|$ among 1.9, 2, 2.2, 3.
- Case 2.** Set $\beta = 80$, choose $\alpha = 0$, $c_1 = 0$, $c_3 = 1$ and $\Omega = (3, 0, 0)^T$. In such a setting, both the elongated direction of the condensate and the rotation axis are parallel to x -axis. We then study the impact of trapping potential on the GS by varying κ among 1, 1.5, 2, 2.5.
- Case 3.** Same as the Case 2 right above by only changing β to a larger one $\beta = 1000$.

Figs. 8–10 depict the isosurface $|\phi_g(x)|^2 = 4 \times 10^{-4}$ for Case 1 while $|\phi_g(x)|^2 = 10^{-3}$ for Case 2 & for Case 3 as well as the corresponding slice plots of $|\phi_g(x)|^2$ perpendicular to rotation axis \mathbf{n} . From these figures and additional numerical results not shown here for brevity, we can see that: (i) Vortex lines are straight if the rotation axis is parallel to the elongated direction of the condensate and rotation is fast enough (cf. Figs. 8 & 10). Moreover, as $|\Omega|$ increases, patterns of GS will transform from vortex lattice to vortex ring (cf. Fig. 8). (ii) For $|\Omega|$ not too large, the GS pattern presents as a torus (cf. Fig. 9). In addition, vortex lines will be brought into the torus and aligned along the direction of rotation axis \mathbf{n} when $|\Omega|$ is large enough (cf. Fig. 10). (iii) The inner diameter of the torus will decrease as the strength of the quartic potential (i.e. κ in (4.1)) increases. Hence for a fixed large enough $|\Omega|$, the GS pattern with vortex ring will shrink into vortex lattice as κ increases (cf. Fig. 10).

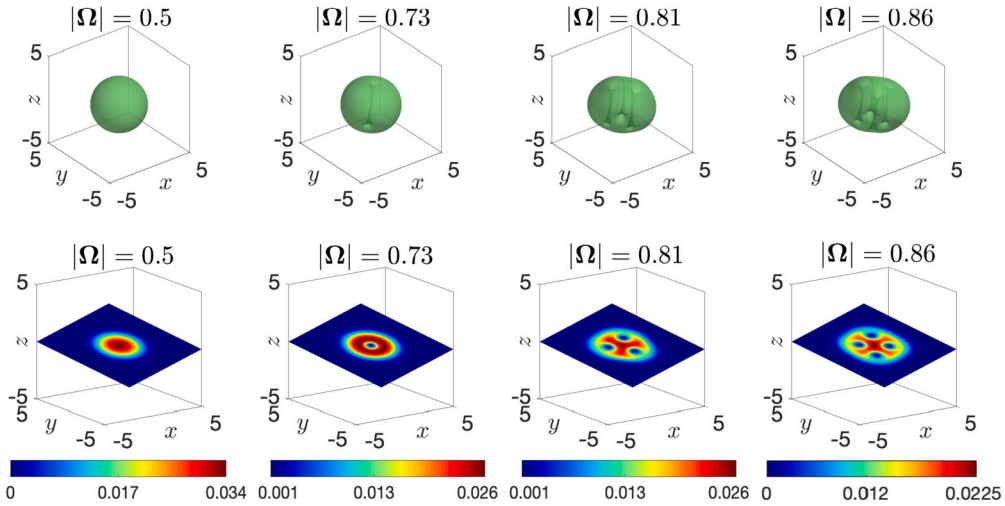


Fig. 6. Isosurface of $|\phi_g(x)|^2 = 10^{-3}$ (upper) and slice of $|\phi_g(x)|^2$ perpendicular to the rotation axis (lower) for Case 2 of Example 4.3.

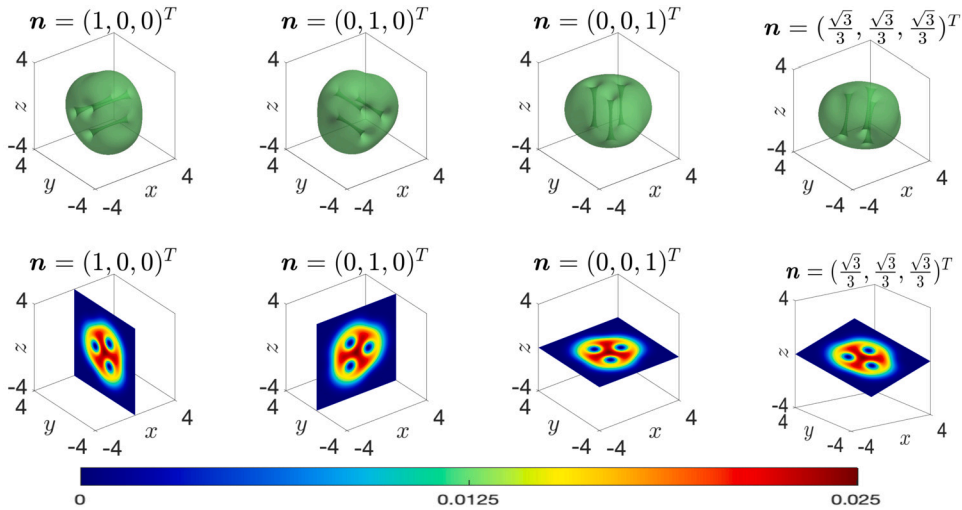


Fig. 7. Isosurface of $|\phi_g(x)|^2 = 10^{-3}$ (upper) and slice of $|\phi_g(x)|^2$ perpendicular to the rotation axis (lower) for Case 3 of Example 4.3.

Example 4.5. Here, we choose potential $V(x)$ as the toroidal trapping potential (4.2). In such potential, the Gaussian part in (4.2) will introduce a repulsive potential barrier hence driving an outward ‘force’. Together with the centrifugal force created by the rotation, this force competing with the centripetal force driven by the harmonic potential in (4.2) will bring ample diversity to the GS patterns. To carry out their impact on the GS patterns, we fix $\beta = 1000$, $n = n_0$ and consider the following three cases:

- Case 1.** Set $|\Omega| = 0$, $a = 0.1$ and vary V_0 among 60, 70, 80, 90.
- Case 2.** Set $|\Omega| = 0.5$, $a = 0.1$ and vary V_0 among 0, 45, 50, 55.
- Case 3.** Set $|\Omega| = 0.5$, $V_0 = 55$ and vary a among 0.104, 0.107, 0.109, 0.3.

Figs. 11–13 show respectively the isosurface $|\phi_g(x)|^2 = 4 \times 10^{-4}$ for Case 1, $|\phi_g(x)|^2 = 10^{-4}$ for Case 2 & $|\phi_g(x)|^2 = 10^{-3}$ for Case 3 as well as the corresponding slice plots of $|\phi_g(x)|^2$ perpendicular to rotation axis n . From these figures and additional numerical results not shown here for brevity, we can see that: (i) For a non-rotating BEC with fixed a in the potential, as the strength of the repulsive outward ‘force’ induced by the Gaussian (i.e. V_0) grows, the GS pattern will transform from a solid ball to a hollow sphere. Meanwhile, both the inner and outer spheres become larger, and the inner diameter increases faster than the outer one (cf. Fig. 11). (ii) For a rotating BEC with fixed a , similar to those in (i), when V_0 is small, the GS pattern presents as a solid ball carrying vortex lines for a sufficiently large $|\Omega|$. As V_0 grows, the number of vortex lines in the GS increases meanwhile the density in the center of the condensates will be gradually expelled out, leading to a GS pattern in the shape of torus carrying vortex lines (cf. Fig. 12). (iii) For rotating BEC with proper fixed V_0 and $|\Omega|$, the GS pattern presents as a torus surrounded by vortex lines parallel to the rotation axis (cf. last column in Fig. 12). Then, decreasing the width of the Gaussian (i.e. increasing a in potential (4.2)), vortex lines in the

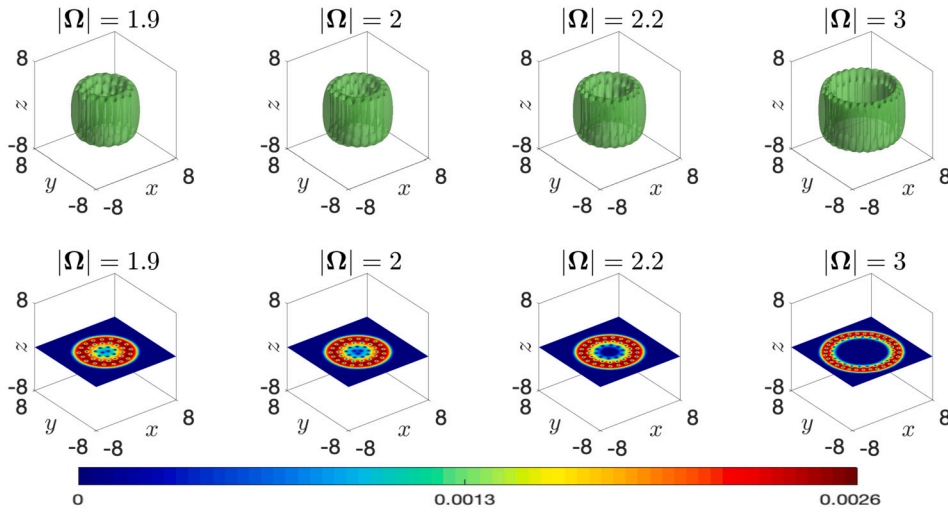


Fig. 8. Isosurface of $|\phi_g(x)|^2 = 4 \times 10^{-4}$ (upper) and slice of $|\phi_g(x)|^2$ perpendicular to the rotation axis with harmonic-plus-quartic potential in Case 1 of Example 4.4.

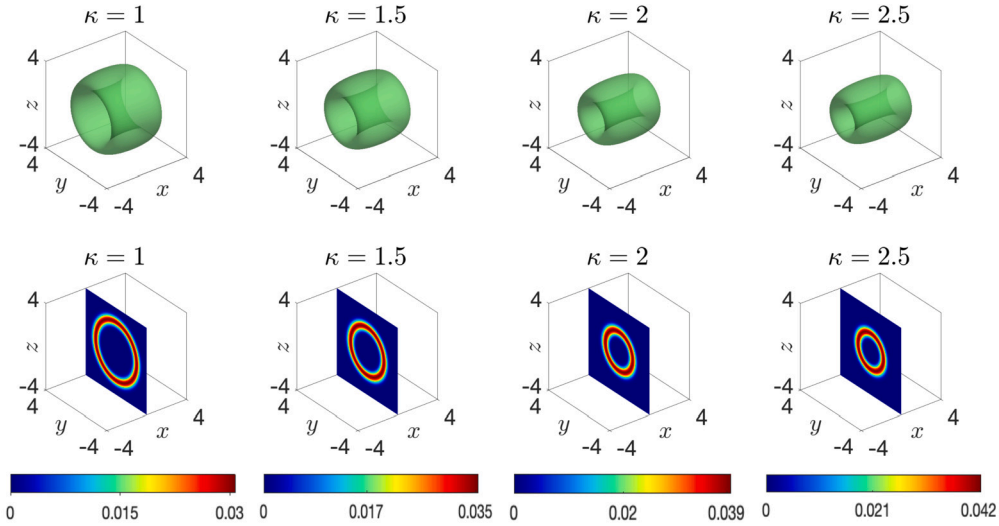


Fig. 9. Isosurface of $|\phi_g(x)|^2 = 10^{-3}$ and slice of $|\phi_g(x)|^2$ perpendicular to the rotation axis with harmonic-plus-quartic potential for Case 2 in Example 4.4.

resulted GS will then gradually vanish, and the GS pattern eventually reduces into a smooth torus without vortices. Moreover, the inner and outer diameters of the torus decrease as a increases (cf. Fig. 13).

5. Conclusion

In this paper, we first study the existence and properties of the ground states for 3D Bose-Einstein condensates with arbitrary-angle rotation. Then, a preconditioned Riemannian conjugate gradient (pRCG) method is proposed to compute the ground states. The pRCG method is accurate, efficient, easy to implement and capable of computing ground states for fast rotating BECs with highly strong nonlinearity under various complicated trapping potentials. Furthermore, we apply pRCG to investigate the ground state patterns with different parameters. Impacts of the trapping potential, the nonlinearity strength, and the angle of the rotation on the GS patterns are carried out in details. Notably, we find that in a mild-rotating system with anisotropic trapping potential, vortex lines are bent. In particular, we observe the U-shaped vortex and S-shaped vortex in a cigar-shaped slow-rotating BEC, which, to our best knowledge, is the first observation in such a system. Other ample GS patterns under different parameter regimes are also explored. Extension of the pRCG method to more general systems, such as the rotating dipolar BEC, is straightforward and provides a powerful tool for investigating properties of GS with various vortex structures, especially for BECs with strong nonlinearity and fast rotation.

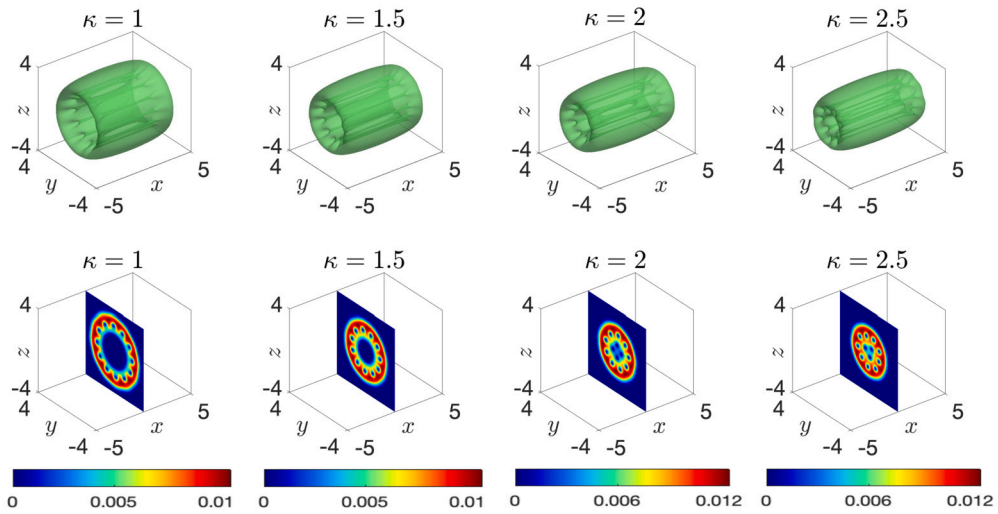


Fig. 10. Isosurface of $|\phi_g(x)|^2 = 10^{-3}$ and slice of $|\phi_g(x)|^2$ perpendicular to the rotation axis with harmonic-plus-quartic potential for Case 3 in Example 4.4.

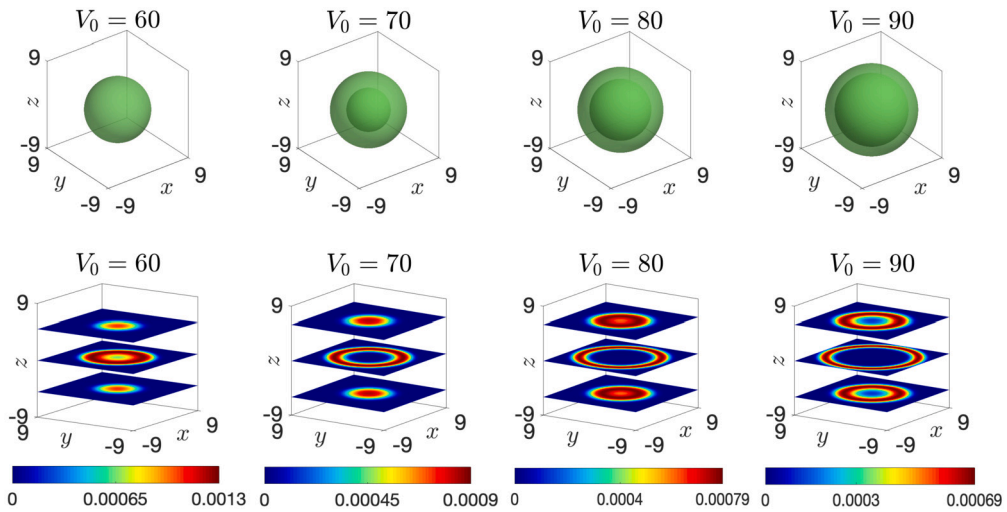


Fig. 11. Isosurface of $|\phi_g(x)|^2 = 4 \times 10^{-4}$ (upper) and slice of $|\phi_g(x)|^2$ perpendicular to the rotation axis with toroidal potential in Case 1 of Example 4.5.

CRedit authorship contribution statement

Qingzhou Shu: Data curation, Formal analysis, Investigation, Methodology, Software, Validation, Visualization, Writing – original draft, Writing – review & editing. **Qinglin Tang:** Conceptualization, Formal analysis, Funding acquisition, Methodology, Project administration, Resources, Supervision, Visualization, Writing – review & editing. **Shaobo Zhang:** Data curation, Formal analysis, Investigation, Software, Validation, Visualization, Writing – original draft, Writing – review & editing. **Yong Zhang:** Conceptualization, Formal analysis, Funding acquisition, Methodology, Resources, Supervision, Writing – review & editing.

Declaration of competing interest

The authors declare that they have no known competing financial interests or personal relationships that could have appeared to influence the work reported in this paper.

Data availability

Data will be made available on request.

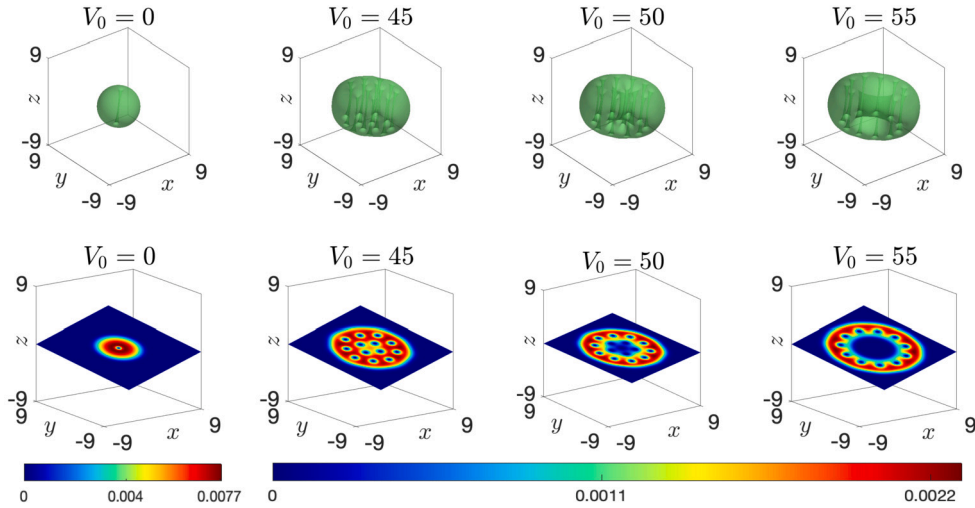


Fig. 12. Isosurface of $|\phi_g(x)|^2 = 10^{-3}$ (upper first figure) & $|\phi_g(x)|^2 = 10^{-4}$ (upper right three figures) and slice of $|\phi_g(x)|^2$ perpendicular to the rotation axis with toroidal potential in Case 2 of Example 4.5.

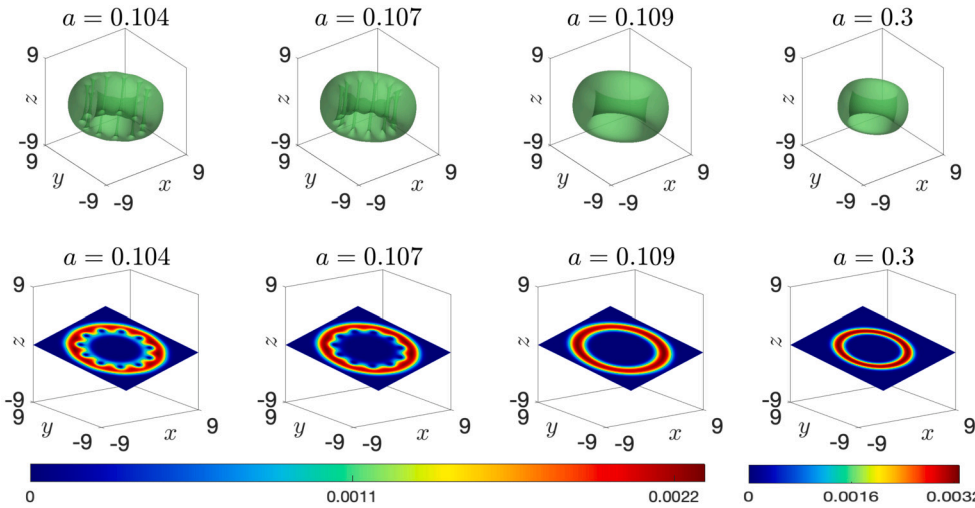


Fig. 13. Isosurface of $|\phi_g(x)|^2 = 10^{-3}$ (upper) and slice of $|\phi_g(x)|^2$ perpendicular to the rotation axis with toroidal potential in Case 3 of Example 4.5.

Acknowledgements

Q. Shu and Q. Tang were supported by the National Natural Science Foundation of China (No. 11971335) and the Institutional Research Fund from Sichuan University (No. 2020SCUNL110). S. Zhang and Y. Zhang were supported by the National Natural Science Foundation of China (No. 12271400), Tianjin Municipal Science and Technology Bureau (No. 22ZYJJJC00020) and Tianyuan Mathematical Center in Southwest China (No. 12226102).

References

- [1] J.R. Abo-Shaeer, C. Raman, J.M. Vogels, W. Ketterle, Observation of vortex lattices in Bose-Einstein condensates, *Science* 292 (2001) 476–479.
- [2] P. Absil, R. Mahony, R. Sepulchre, *Optimization Algorithms on Matrix Manifolds*, Princeton University Press, 2008.
- [3] A. Aftalion, Q. Du, Vortices in a rotating Bose-Einstein condensate: critical angular velocities and energy diagrams in the Thomas-Fermi regime, *Phys. Rev. A* 64 (2001) 063603.
- [4] A. Aftalion, T. Riviere, Vortex energy and vortex bending for a rotating Bose-Einstein condensate, *Phys. Rev. A* 64 (2001) 043611.
- [5] M.H. Anderson, J.R. Ensher, M.R. Matthews, C.E. Wieman, E.A. Cornell, Observation of Bose-Einstein condensation in a dilute atomic vapor, *Science* 269 (1995) 198–201.
- [6] X. Antoine, C. Besse, R. Duboscq, V. Rispoli, Acceleration of the imaginary time method for spectrally computing the stationary states of Gross-Pitaevskii equations, *Comput. Phys. Commun.* 219 (2017) 70–78.
- [7] X. Antoine, R. Duboscq, Modeling and computation of Bose-Einstein condensates: stationary states, nucleation, dynamics, stochasticity, in: C. Besse, J.C. Garreau (Eds.), *Nonlinear Optical and Atomic Systems: At the Interface of Physics and Mathematics*, Lect. Notes Math. 2146 (2015) 49–145.

- [8] X. Antoine, R. Duboscq, Robust and efficient preconditioned Krylov spectral solvers for computing the ground states of fast rotating and strongly interacting Bose-Einstein condensates, *J. Comput. Phys.* 258 (2014) 509–523.
- [9] X. Antoine, A. Levitt, Q. Tang, Efficient spectral computation of the stationary states of rotating Bose-Einstein condensates by preconditioned nonlinear conjugate gradient methods, *J. Comput. Phys.* 343 (2017) 92–109.
- [10] X. Antoine, Q. Tang, Y. Zhang, A preconditioned conjugated gradient method for computing ground states of rotating dipolar Bose-Einstein condensates via kernel truncation method for dipole-dipole interaction evaluation, *Commun. Comput. Phys.* 24 (2018) 966–988.
- [11] W. Bao, Y. Cai, Mathematical theory and numerical methods for Bose-Einstein condensation, *Kinet. Relat. Models* 6 (2013) 1–135.
- [12] W. Bao, Q. Du, Computing the ground state solution of Bose-Einstein condensates by a normalized gradient flow, *SIAM J. Sci. Comput.* 25 (2004) 1674–1697.
- [13] W. Bao, W. Tang, Ground state solution of Bose-Einstein condensate by directly minimizing the energy functional, *J. Comput. Phys.* 187 (2003) 230–254.
- [14] W. Bao, H. Wang, P.A. Markowich, Ground, symmetric and central vortex states in rotating Bose-Einstein condensates, *Commun. Math. Sci.* 3 (2005) 57–88.
- [15] W. Bao, Y. Zhang, Dynamics of the ground state and central vortex state in Bose-Einstein condensation, *Math. Models Methods Appl. Sci.* 15 (2005) 1863–1896.
- [16] I. Bialynicki-Birula, Z. Bialynicka-Birula, Center-of-mass motion in the many-body theory of Bose-Einstein condensates, *Phys. Rev. A* 65 (2002) 063606.
- [17] C.C. Bradley, C.A. Sackett, J.J. Tollett, R.G. Hulet, Evidence of Bose-Einstein condensation in an atomic gas with attractive interactions, *Phys. Rev. Lett.* 75 (1995) 1687–1690.
- [18] V. Bretin, S. Stock, Y. Seurin, J. Dalibard, Fast rotation of a Bose-Einstein condensate, *Phys. Rev. Lett.* 92 (2004) 050403.
- [19] H. Chen, G. Dong, W. Liu, Z. Xie, Second-order flows for computing the ground states of rotating Bose-Einstein condensates, *J. Comput. Phys.* 475 (2023) 111872.
- [20] I. Danaïla, P. Kazemi, A new Sobolev gradient method for direct minimization of the Gross-Pitaevskii energy with rotation, *SIAM J. Sci. Comput.* 32 (2010) 2447–2467.
- [21] I. Danaïla, B. Protas, Computation of ground states of the Gross-Pitaevskii functional via Riemannian optimization, *SIAM J. Sci. Comput.* 39 (2017) B1102–B1129.
- [22] K.B. Davis, M.O. Mewes, M.R. Andrews, N.J. van Druten, D.S. Durfee, D.M. Kurn, W. Ketterle, Bose-Einstein condensation in a gas of sodium atoms, *Phys. Rev. Lett.* 75 (1995) 3969–3973.
- [23] C.M. Dion, E. Cancès, Ground state of the time-independent Gross-Pitaevskii equation, *Comput. Phys. Commun.* 177 (2007) 787–798.
- [24] J.J. García-Ripoll, V.M. Pérez-García, Vortex bending and tightly packed vortex lattices in Bose-Einstein condensates, *Phys. Rev. A* 64 (2001) 053611.
- [25] J.J. García-Ripoll, V.M. Pérez-García, Vortex nucleation and hysteresis phenomena in rotating Bose-Einstein condensates, *Phys. Rev. A* 63 (2001) 041603(R).
- [26] E. Hodby, S.A. Hopkins, G. Hechenblaikner, N.L. Smith, C.J. Foot, Experimental observation of a superfluid gyroscope in a dilute Bose-Einstein condensate, *Phys. Rev. Lett.* 91 (2003) 090403.
- [27] E.H. Lieb, R. Seiringer, J. Yngvason, Bosons in a trap: a rigorous derivation of the Gross-Pitaevskii energy functional, *Phys. Rev. A* 61 (2000) 043602.
- [28] W. Liu, Y. Cai, Normalized gradient flow with Lagrange multiplier for computing ground states of Bose-Einstein condensates, *SIAM J. Sci. Comput.* 43 (2021) B219–B242.
- [29] J. Nocedal, S.J. Wright, *Numerical Optimization*, second edition, Springer, 2006.
- [30] S.B. Prasad, B.C. Mulkerin, A.M. Martin, Arbitrary-angle rotation of the polarization of a dipolar Bose-Einstein condensate, *Phys. Rev. A* 103 (2021) 033322.
- [31] S.B. Prasad, B.C. Mulkerin, A.M. Martin, Stationary states, dynamical stability, and vorticity of Bose-Einstein condensates in tilted rotating harmonic traps, *Phys. Rev. A* 101 (2020) 063608.
- [32] C. Ryu, M.F. Andersen, P. Cladé, V. Natarajan, K. Helmerson, W.D. Phillips, Observation of persistent flow of a Bose-Einstein condensate in a toroidal trap, *Phys. Rev. Lett.* 99 (2007) 260401.
- [33] R. Seiringer, Gross-Pitaevskii theory of the rotating Bose gas, *Commun. Math. Phys.* 229 (2002) 491–509.
- [34] L. Simon, Asymptotics for a class of nonlinear evolution equations, with applications to geometric problems, *Ann. Math.* 118 (1983) 525–571.
- [35] S.T. Smith, Optimization techniques on Riemannian manifolds, *Fields Inst. Commun.* 3 (1994) 113–135.
- [36] N.L. Smith, W.H. Heathcote, L.M. Krueger, C.J. Foot, Experimental observation of the tilting mode of an array of vortices in a dilute Bose-Einstein condensate, *Phys. Rev. Lett.* 93 (2004) 080406.
- [37] S. Stringari, Superfluid gyroscope with cold atomic gases, *Phys. Rev. Lett.* 86 (2001) 4725–4728.
- [38] G. Vergez, I. Danaïla, S. Auliac, F. Hecht, A finite-element toolbox for the stationary Gross-Pitaevskii equation with rotation, *Comput. Phys. Commun.* 209 (2016) 144–162.
- [39] Y. Wang, B. Jeng, C. Chien, A two-parameter continuation method for rotating two-component Bose-Einstein condensates in optical lattices, *Commun. Comput. Phys.* 13 (2013) 442–460.
- [40] X. Wu, Z. Wen, W. Bao, A regularized Newton method for computing ground states of Bose-Einstein condensates, *J. Sci. Comput.* 73 (2017) 303–329.
- [41] Q. Zhuang, J. Shen, Efficient SAV approach for imaginary time gradient flows with applications to one- and multi-component Bose-Einstein condensates, *J. Comput. Phys.* 396 (2019) 72–88.